Materials and Design 189 (2020) 108532

Contents lists available at ScienceDirect

Materials and Design

journal homepage: www.elsevier.com/locate/matdes

Mechanical performance and corrosion behaviour of Zr-based bulk metallic glass produced by selective laser melting

L. Deng [a,*], A. Gebert [a], L. Zhang [c], H.Y. Chen [a,d], D.D. Gu [d], U. Kühn [a], M. Zimmermann [b], K. Kosiba [a], S. Pauly [a,e]

[a] Institute for Complex Materials, IFW Dresden, Helmholtzstraße 20, D-01069 Dresden, Germany
[b] Institute of Materials Science, Faculty of Mechanical Engineering, TU Dresden, D-01062 Dresden, Germany
[c] Shenyang National Laboratory for Materials Science, Institute of Metal Research, Chinese Academy of Science, 72 Wenhua Road, Shenyang 110016, PR China
[d] College of Materials Science and Technology, Nanjing University of Aeronautics and Astronautics, Yudao Street 29, Nanjing 210016, Jiangsu Province, People's Republic of China
[e] University of Applied Sciences Aschaffenburg, Würzburger Straße 45, D-63743 Aschaffenburg, Germany

HIGHLIGHTS

- $Zr_{52.5}Cu_{17.9}Ni_{14.6}Al_{10}Ti_5$ glass with a relative density exceeding 98.7% is fabricated via selective laser melting (SLM).
- The samples deform plastically (about 0.5%) and have high yield strengths above 1700 MPa in compression.
- Microhardness maps of SLM specimens suggest structural homogeneity despite the complex thermal history.
- The wear performance and corrosion properties of the SLM samples are comparable to that of the as-cast glass.
- SLM allows fabrication of metallic glasses, which can withstand the conditions arising in real-world applications.

GRAPHICAL ABSTRACT

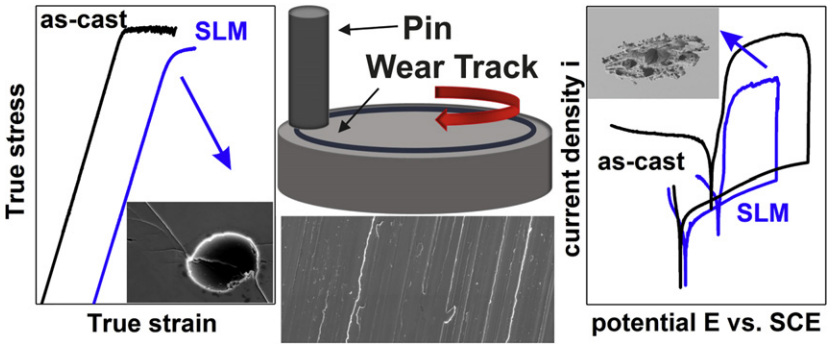

ARTICLE INFO

Article history:
Received 22 August 2019
Received in revised form 28 January 2020
Accepted 29 January 2020
Available online 30 January 2020

Keywords:
Selective laser melting
Zr-based alloy
Microhardness
Compression tests
Wear resistance
Corrosion resistance

ABSTRACT

Nearly fully dense, glassy $Zr_{52.5}Cu_{17.9}Ni_{14.6}Al_{10}Ti_5$ bulk specimens were fabricated by selective laser melting (SLM) and their behaviour during compressive loading, during wear testing and in a corrosive medium was investigated. Their performance was compared with as-cast material of the same composition. The additively manufactured samples exhibit a yield strength around 1700 MPa combined with a plastic strain of about 0.5% after yielding despite the residual porosity of 1.3%, which is distributed uniformly in the samples. The propagation of shear bands in the bulk metallic glass prepared by SLM was studied. The specific wear rate and the worn surfaces demonstrated that similar wear mechanisms are active in the SLM and the as-cast samples. Hence, manufacturing the glass in layers does not adversely affect the wear properties. The same holds for the corrosion tests, which were carried out in 0.01 M Na_2SO_4 and 0.1 M NaCl electrolyte. The anodic polarization curves of SLM samples and as-cast samples revealed a similar corrosion behaviour. However, the SLM samples have a slightly reduced susceptibility to pitting corrosion and exhibit an improved surface healing ability, which might be attributed to an improved homogeneity of the additively manufactured glass.

1. Introduction

Selective laser melting (SLM), an additive manufacturing technique (powder bed fusion), has attracted a lot of attention as a promising

* Corresponding author.
E-mail address: l.deng@ifw-dresden.de (L. Deng).

https://doi.org/10.1016/j.matdes.2020.108532

method for processing a wide variety of metallic materials [1,2]. Owing to the concept of producing a component layer by layer and because of the resulting intrinsically high cooling rates (10^3–10^8 K/s) [3], the materials properties can be significantly modified leading to, for example, unexpected high strengths [4]. Such high cooling rates are also inevitable for obtaining a glassy state from a metallic melt and, consequently, glass-forming alloys have been prepared by means of various additive-manufacturing techniques [5,6]. The approach to prepare bulk metallic glasses (BMGs) by SLM bears the indisputable advantage that the size of the additively manufactured glassy components can exceed the typical dimensions of cast bulk metallic glasses, which are generally limited to a few millimetres [7]. Simultaneously, also delicate and complex geometries can be obtained, which are otherwise inaccessible to conventional melt quenching techniques [8]. This is very promising in terms of practical applications of BMGs, which are largely restricted by their small as well as usually simple geometries [7]. Because of this unique potential, different glass-forming alloys such as Fe-, Zr-, Ti- and Al-based alloys have been processed by SLM, to date [9–19].

Like for all materials, the synthesis and processing details themselves have a strong bearing on the properties and behaviour of (bulk) metallic glasses. The layer-by-layer processing can lead to chemical or structural heterogeneities [20,21] and an elevated concentration of pores [11,12]. An important question in this context, consequently, is how additively manufactured metallic glasses perform under conditions, which arise in applications, and whether or not, they behave in a different manner than as-cast glasses. In this work, we are interested in clarifying this by specifically concentrating on the mechanical and corrosion behaviour of a Zr-based bulk metallic glass.

While all bulk metallic glasses suffer from an almost complete lack of tensile ductility [22,23], some glass formers are malleable upon compressive loading [22]. Especially Zr-based glasses are known to plastically deform by a few percent, which is a prerequisite for any engineering application. Moreover, BMGs are very attractive for applications involving contact sliding [24–26]. It has been reported that Ni-based BMGs have a much higher durability than conventional carbon tool steels [27]. Zr-based, Cu-based and Ti-based BMGs also show excellent wear resistance [26,28–33]. Huang et al. have demonstrated that the cooling rate is one important parameter for the wear performance of BMGs [29]. Since SLM generally yields much higher cooling rates than copper mould casting [3], one can anticipate differences in the wear behaviour. In addition, the presence of μm-scale pores in the SLM samples might also play an important role. Yet, data on these aspects are still scarce [14] and the detailed mechanism has not been explored.

Another crucial point in terms of potential applications is the corrosion behaviour of BMGs produced by SLM. Cast bulk metallic glasses, in particular transition metal-based bulk-glass forming alloys, such as Zr-Cu-based multicomponent alloys, have been subject of numerous fundamental corrosion studies [34–39]. In water-based solutions, they exhibit low free corrosion rates and spontaneous and stable anodic passivation, both generally superior to crystalline alloys with comparable compositions [40]. This is due to the formation of very thin barrier-type oxide layers, which are mainly composed of valve-metal oxides (Zr-, Ti-, Nb-, Al-oxides) [39,41,42]. The chemically homogeneous nature of a monolithic glassy state is another reason for the enhanced corrosion resistance [43–45]. However, as-cast glassy samples are very sensitive to pitting corrosion related to fast pit propagation and low repassivation abilities. The reasons for pit initiation are structural defects due to non-ideal casting conditions or defects (e.g. notches and scratches) at the sample surface [36]. Once pitting has commenced, pits grow rapidly into the reactive metastable phase. Especially Cu is a critical alloying element in this regard because it increases the pitting susceptibility and deteriorates the repassivation ability in Zr-based BMGs [39]. The powder used for additive manufacturing might suffer from chemical heterogeneities and the SLM process imposes completely different solidification conditions on the metallic melt. They could even promote chemical heterogeneities and with it structural heterogeneities (e.g. crystalline precipitates) [46]. The oxygen uptake during SLM process may also influence the corrosion resistance of SLM samples [47]. In addition, pores are present after selective laser melting and all these factors are expected to impact the corrosion behaviour.

We produced glassy $Zr_{52.5}Cu_{17.9}Ni_{14.6}Al_{10}Ti_5$ specimens with a high relative density by SLM in the present work. The same set of additively manufactured, fully glassy specimens is used to systematically investigate the interrelation between processing and properties. This covers investigation of structural heterogeneity, corrosion properties, wear and deformation behaviour on uniaxial compression. Since we are interested in the mechanical properties of monolithic bulk metallic glasses, which exhibit zero ductility in tension, we solely concentrate on compression tests. Only when the performance of the bulk metallic glass is not adversely affected by additive manufacturing, can selective laser melting of glass-forming alloys be considered a viable route for the production of bulk metallic glasses on a larger scale, e.g. for commercial applications. Therefore, comprehensive characterization of bulk metallic glasses obtained by SLM combined with a direct comparison with as-cast material of the same composition is of paramount importance. Our results prove that selectively laser-melted $Zr_{52.5}Cu_{17.9}Ni_{14.6}Al_{10}$ are able to compete with as-cast samples of the same composition.

2. Material and method

The $Zr_{52.5}Cu_{17.9}Ni_{14.6}Al_{10}Ti_5$ (at.%) ingots were prepared in an arc melter (Edmund Bühler GmbH) in a Ti-gettered Ar atmosphere. All constituent elements with a purity exceeding 99.9 wt% were cleaned prior to melting. Each ingot was re-melted four times to ensure chemical homogeneity. Afterwards, the ingots were gas-atomized by Nanoval GmbH & Co. KG via electrode induction-melting gas atomization (EIGA). The particle size distribution was obtained by using dynamic image analysis (CAMSIZER X2, Retsch TECHNOLOGY). After sieving, a particle size below 90 μm was chosen for selective laser melting ($d_{10} = 17 \pm 1$ μm, $d_{90} = 71 \pm 1$ μm). The SLM samples were prepared in a SLM 50 system (Realizer GmbH) equipped with a fibre laser (spot size: 50 μm). A laser power of 109.5 W, a scanning speed of 1000 mm/s, a layer thickness of 40 μm and a hatch distance of 200 μm was employed. The unidirectional scanning vectors were rotated by 90° in adjacent layers. These parameters represent an optimized process compared to our previous experiments [11]. The oxygen content was kept below 0.01 vol% by purging the SLM chamber with Ar during the process. Cylindrical samples with a length of 6 mm and a diameter of 3 mm were prepared as well as rectangular specimens ($3 \times 3 \times 6$ mm^3). In addition, rods with a length of 35 mm and a diameter of 3 mm were obtained by suction casting in an arc melter (Edmund Bühler GmbH) using the aforementioned ingots. These dimensions were chosen to ensure complete vitrification of the $Zr_{52.5}Cu_{17.9}Ni_{14.6}Al_{10}Ti_5$ melt on quenching [48].

The chemical composition and the oxygen content of the $Zr_{52.5}Cu_{17.9}Ni_{14.6}Al_{10}Ti_5$ powder and the SLM specimens were measured using ICP-OES (inductively-coupled plasma-optical emission spectroscopy, IRIS Intrepid II XUV from Thermo Fischer Scientific GmbH) and carrier gas hot extraction (TC-436DR, LECO), respectively. The composition of three independent powder batches was analyzed. The XRD samples with a thickness between 90 and 100 μm were cut from the rods and ground. X-ray diffraction (XRD) was carried out on a STOE STADIP diffractometer (STOE & Cie GmbH) with Mo-$K_{\alpha 1}$ radiation ($\lambda = 0.07093187$ nm) in transmission mode. The differential scanning calorimetry (DSC) specimens with a weight of about 17 mg were measured at a heating rate of 0.33 K/s in a Perkin-Elmer Diamond calorimeter. The density of the SLM samples was determined by the Archimedean principle using a Sartorius balance (MSA 225S). X-ray computed tomography (μ-CT, Phoenix nanotom m, General Electric) was conducted at 130 kV and 100 μA with a voxel size of 3 μm to analyze the volume fraction and distribution of pores. Additional structural characterization

was carried out on a FEI Tecnai F20 transmission electron microscope (TEM) equipped with a field-emission gun. The TEM samples were mechanically ground to 30 μm and dimpled to 10 μm, followed by ion-milling until perforation with a Gatan 691 device under liquid nitrogen cooling.

Both cylindrical SLM and as-cast samples with a length of 6 mm and a diameter of 3 mm were prepared for the uniaxial compression tests. The faces of the cylinders were ground to ensure that they are perpendicular to the cylinder axis. To further investigate the propagation of shear bands, one lateral side of the rectangular SLM samples was polished prior to loading to fracture. Room-temperature compression tests were conducted at a constant crosshead velocity corresponding to an initial strain rate of 2×10^{-4} s^{-1} in an Instron 5869 and at least three specimens for each state were compressed. The strain was directly monitored at the sample using a laser extensometer (Fiedler Optoelektronik GmbH). Vickers microhardness measurements were performed on polished samples using an HMV Shimadzu Microhardness tester. Indents were made with a load of 200 g and 10 s of dwell time. The distance between the individual indents with a typical diagonal of around 30 μm was 100 μm. Pin-on-disk friction tests were carried out by a Tribometer (T500, Nanovea) at room temperature. The cylindrical samples with a length of 20 mm and a diameter of 3 mm, whose surfaces were ground to 4000 grit with SiC abrasive paper, and an X210Cr12 steel friction pair were performed with a load of 15 N applied on the pin, a 15 mm radius of the wear track, a rotating speed of 240 rpm and a sliding duration of 480 min. The tests for each sliding duration were done at least 3 times.

The rod specimens with a length of 10 mm and a diameter of 3 mm diameter were electrically connected and embedded in epoxy resin for electrochemical measurements. The cross section, the only part exposed to the corrosive environment of the samples was ground to 4000 grid, afterwards the interfaces between the sample and the epoxy resin were coated with a varnish to avoid crevice corrosion. Usually a small crevice forms between resin and the metal after grinding, which can cause undesired local (crevice) corrosion. This is not representative of the behaviour of the bulk glassy material [38] and, hence, constitutes an artefact. All polarization tests were performed at ambient temperature in a 0.01 M Na_2SO_4 and 0.1 M NaCl solution with pH 6.5. This electrolyte has been identified in our lab as suitable for electrochemical corrosion analysis of Zr-based metallic glass samples and, consequently, it has already been frequently employed for similar studies [35–38,41]. For the measurements, a Solartron SI1287 electrochemical interface was used, which was connected to a standard three-electrode cell with $Zr_{52.5}Cu_{17.9}Ni_{14.6}Al_{10}Ti_5$ specimens as working electrode, a saturated calomel electrode (SCE, E (SHE) = 0.241 V) as the reference electrode and a Pt-net as the counter electrode. To ensure that the samples have reproducible surface states, after grinding they were exposed to air with a relative humidity of around 30% at room temperature for 20 h before they were tested in the electrolyte. The specimens were immersed in the solution for 30 min while monitoring the open circuit potential (OCP). Potentiodynamic polarization measurements were conducted using a scan rate of 0.5 mV/s up to anodic potential values slightly beyond the pitting potential. The polarization direction was reversed when the measured anodic current density reached a defined value of 1 mA/cm^2. The measurement was stopped at −0.5 V versus OCP. Each test was repeated at least 5 times for both SLM and as-cast samples in order to assess the repeatability of the results. By means of graphical extrapolation analysis from each measured curve, the characteristic parameters were determined: the corrosion potential, E_{corr}, the corrosion current density, i_{corr}, the pitting potential, E_{pit}, and the repassivation potential, E_R.

The gas-atomized powder particles, the fracture morphologies, the worn surfaces after friction testing and the pitted areas after polarization test were investigated in a scanning electron microscope (SEM, Gemini 1530, Carl Zeiss AG).

3. Results and discussion

The gas-atomized powder has a composition of $Zr_{52.3}Cu_{18}Ni_{14.6}Al_{10.1}Ti_5$ (at.%), which is in excellent agreement with the nominal composition of $Zr_{52.5}Cu_{17.9}Ni_{14.6}Al_{10}Ti_5$ (at.%), suggesting that gas atomization does not significantly change the composition of the present alloy. The oxygen content of the original alloy powder (487 ± 5 ppm) is significantly lower than that of the samples after SLM processing (920 ± 20 ppm). Apparently, residual oxygen in the chamber is absorbed during SLM processing due to the high affinity and solution ability of Zr and Ti for oxygen [49,50]. In addition, due to the low oxygen content in the arc melter, the oxygen content of the as-cast sample is only 77 ± 5 ppm.

Fig. 1 (a) depicts the particle size distribution of the sieved $Zr_{52.5}Cu_{17.9}Ni_{14.6}Al_{10}Ti_5$ powder. Knowledge of the powder size distribution is inevitable for designing the proper layer thickness and hatch distance. The majority of the particles has a diameter ranging between 20 and 50 μm. The morphology of the powder particles shown in Fig. 1(b) indicates that only some particles have an irregular, non-spherical shape. Moreover, some satellites sticking to the relatively large particles and powder agglomerates are visible, which is typical of gas-atomized powder. Yet, these phenomena are not so pronounced as to adversely affect the flowability of the powder in the present case [51,52].

The relative density of all SLM samples exceeds 98.7%, which was measured using the Archimedean method. The corresponding XRD patterns of the different samples are displayed in Fig. 2 (a). Neither in the XRD patterns of the cross section of the SLM sample nor in the pattern of the powder (Fig. 2 (a)) sharp reflections indicating the presence of crystalline phases, can be observed. Instead, only a broad scattering maximum is visible, as found for the as-cast sample. Consequently, bulk amorphous $Zr_{52.5}Cu_{17.9}Ni_{14.6}Al_{10}Ti_5$ samples were fabricated by SLM. To obtain more details about the glassy nature, the samples were analyzed in a differential scanning calorimeter. Fig. 2 (b) displays the DSC traces of a SLM sample, of an as-cast sample as well as of the powder. The glass-transition temperature (T_g) and the crystallization temperature (T_x) are marked by arrows. All samples show a characteristic glass transition and a supercooled liquid region prior to crystallization.

While the as-cast sample exhibits a small but distinct pre-peak prior to the strong, second exothermic event, this peak becomes a shoulder in case of the powder and the SLM sample. This could be caused by the significantly higher oxygen content, which is known to stimulate the precipitation of the big cube phase [53,54]. However, the crystallization enthalpies of all samples are identical within the experimental error (SLM: $\Delta H_{cryst} = 55 \pm 2$ J/g; as-cast: $\Delta H_{cryst} = 54 \pm 2$ J/g; powder: $\Delta H_{cryst} = 52 \pm 2$ J/g), so we can assume that all specimens are indeed fully glassy and that no crystals precipitate in the additively manufactured material. This corroborates our XRD analysis.

In order to further characterize the structural state of the SLM samples, transmission electron microscopy was carried out. A representative bright-field TEM micrograph and a corresponding selected area electron diffraction (SAED) pattern are displayed in Fig. 2 (c). The bright-field TEM image reveals a homogeneous maze-like pattern. Moreover, the SAED pattern (shown as inset) exhibits broad and diffuse rings. These results strongly indicate that the SLM sample is fully amorphous, which is in agreement with the results obtained by XRD and DSC.

Fig. 3 (a) shows the defect size (i.e. pore size) distribution and a full μ-CT reconstruction of a representative SLM sample selected for the compression test. The pores distribute uniformly across the sample and no pore aggregation can be found, which is different from our previous work [11]. During SLM, the formation of pores is inevitable. There are many factors, which influence the formation of defects such as the powder deposition itself, the laser power distribution and the quality of the powder particles [52]. A slightly enhanced laser power in combination with an optimized scanning velocity apparently reduces the likelihood to locally not melt powder particles. In addition, the proper

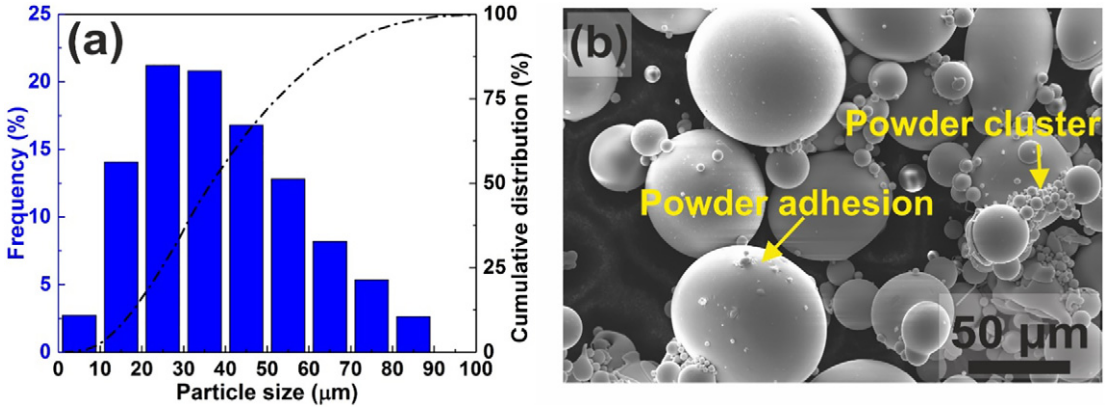

Fig. 1. (a) Particle size distribution of the $Zr_{52.5}Cu_{17.9}Ni_{14.6}Al_{10}Ti_5$ powder after sieving. The powder diameters mainly distribute between 20 and 50 μm. (b) Scanning electron micrograph of the sieved gas-atomized powder. Some particles display non-spherical shapes. Especially the fine particles tend to form satellites and to agglomerate.

amount of relatively small powder particles increases the packing density in the powder bed.

The pore size ranges from 10 μm to 70 μm in the present case. Most of the defects exhibit a spherical geometry, which reveals that the energy input is sufficient. Furthermore, the largest fraction of pores has dimensions below 35 μm, indicating that the optimized parameter can eliminate pore aggregation and decrease the average defect size.

Afterwards, the SLM samples and as-cast samples were uniaxially compressed. Fig. 3(b) depicts the three representative stress-strain curves for the rectangular and the cylindrical SLM samples (dimension of Ø3 mm × 6 mm) as well as for the as-cast sample. The as-cast samples yield at a stress of 1830 ± 50 MPa and show a distinct plastic strain of about 1.5%. The cylindrical SLM samples show a comparatively lower yield stress of about 1710 ± 40 MPa and a typical plastic strain of around 0.5%. The rectangular SLM specimen yields at lower stresses of 1420 ± 20 MPa and fails at stress of 1540 ± 10 MPa with very limited irreversible flow. Both stresses are lower than the ones of the cylindrical samples. Since they were produced with the same process parameters, the defect size and distribution of them is similar, and, therefore, the stress concentrations arising at the edges must be responsible for yielding at lower stresses and the deteriorated plastic deformability [55].

The fracture surfaces of the SLM samples were subsequently investigated in a scanning electron microscope (Figs. 3(c) to (f)). The fracture surface is rather smooth and forms a distinct plane inclined by 45° (inset of Fig. 3(c)) with respect to the loading axis. This is quite different from previous investigations, in which the fracture surface is not a single plane but is reminiscent of an inclined rooftop [12,19]. This means that the stress state is different in the present SLM samples and reveals that they predominantly fail in a shear mode [23]. Multiple interlaced planes form only at the edges of the rods, which cannot be found in the as-cast samples (not shown here). At higher magnifications (Fig. 3(d)), it becomes obvious that the areas around the pores have a more rugged morphology possibly due to the different stress state during compression [11]. Moreover, the vein-like pattern, which is characteristic of shear fracture of as-cast BMGs [23] is found in pore-free regions (inset of Fig. 3(d)), suggesting that the lower porosity contributes to the enhanced plasticity.

To better understand the deformation mechanism of the SLM samples, the polished lateral surface of rectangular specimens after fracture was observed in the SEM. Given the layer-by-layer-fabricated glassy structure of SLM-BMGs, one would expect "interfaces" (about 40 μm thick, Fig. 3(e)) between the individual melt tracks, as it is typically found in conventional alloys and metallic glasses after SLM processing [20,21,46]. One could conjecture that they affect the propagation of shear bands. However, in Fig. 3(e), only straight shear bands can be observed, and they form an angle of 45° with respect to the loading axis. The propagation of shear bands is very sensitive to structural heterogeneities of the glassy structure [56,57]. During the activation of shear transformation zones (STZs), antisymmetric stress-fields evolve ahead of the shear band tip and they are transferred to adjacent non-activated STZs [58]. Both processes are very susceptible to the presence of structural heterogeneities even when the structure remains

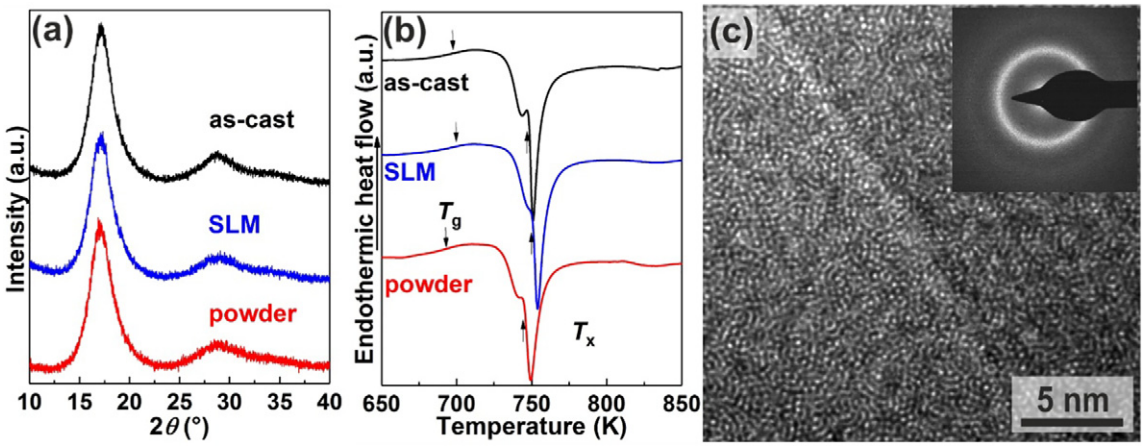

Fig. 2. (a) X-ray diffraction patterns of the $Zr_{52.5}Cu_{17.9}Ni_{14.6}Al_{10}Ti_5$ powder, as-cast and SLM rods with a diameter of 3 mm. Only broad diffraction maxima can be observed, suggesting a fully amorphous structure. (b) DSC traces of representative powder, as-cast and SLM samples. The endothermic glass transition (T_g, marked by arrows) is followed by exothermic crystallization. (c) TEM micrograph and corresponding SAED pattern (inset) of a SLM sample. A homogeneous maze-like pattern reveals a fully glassy structure for the SLM specimen. The broad and diffuse rings shown in the inset corroborate this finding.

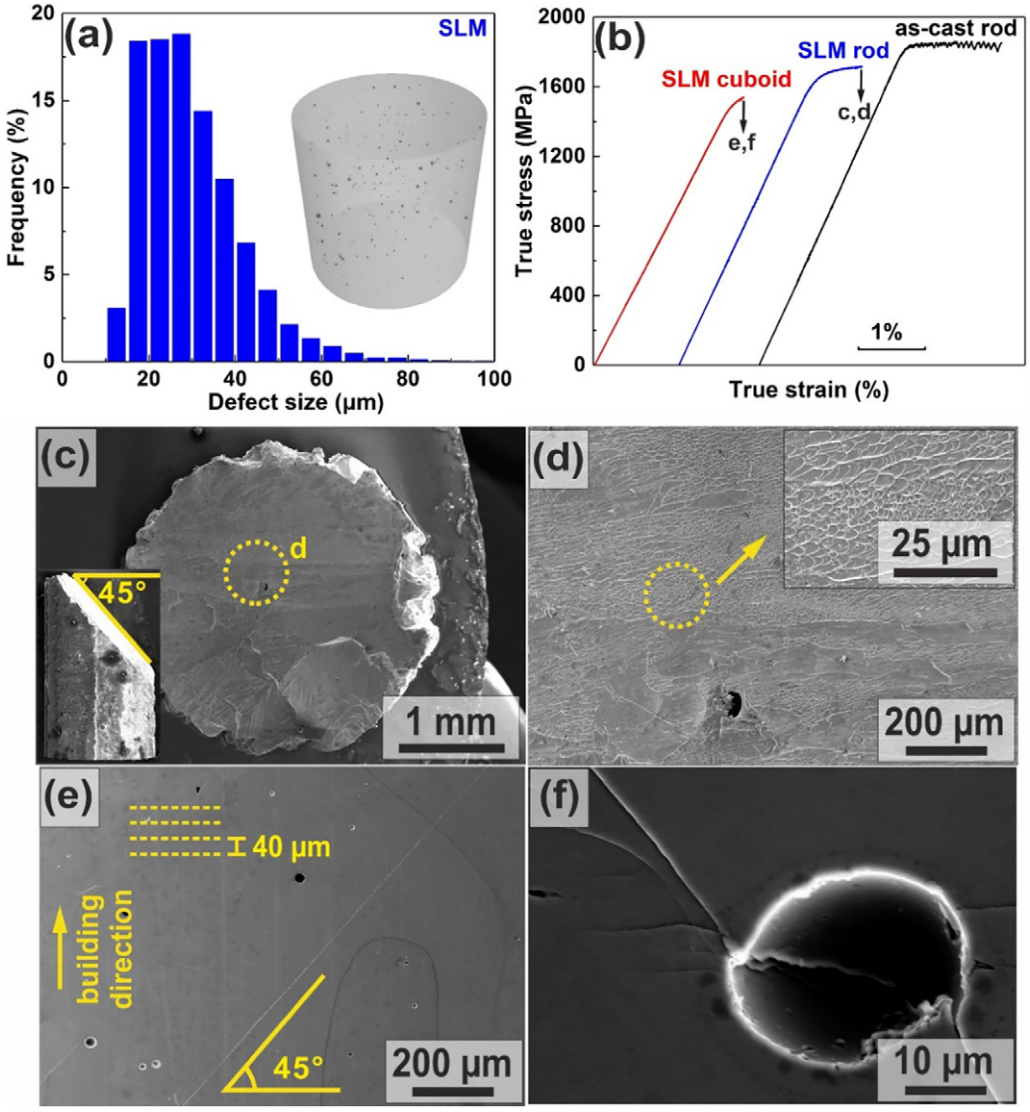

Fig. 3. (a) Defect size distribution and μ-CT reconstruction (inset) of a $Zr_{52.5}Cu_{17.9}Ni_{14.6}Al_{10}Ti_5$ sample produced by SLM. The pore size is randomly distributed within the sample. (b) Three representative stress-strain curves of $Zr_{52.5}Cu_{17.9}Ni_{14.6}Al_{10}Ti_5$ samples prepared by casting and SLM. Both rectangular and rod-shaped SLM samples yield at stresses lower than the as-cast material and exhibit a smaller plastic strain. (c) Fracture surfaces of the rod samples fabricated via SLM. The fracture angle is about 45° (inset). The morphology of the fracture surfaces reveals interlaced fracture planes. (d) Magnified section of the fracture surface shown in (c). The morphology around the pore differs from the residual fracture surface. Typical vein-like patterns are found in pore-free regions (inset). (e) A straight shear band observed on the lateral surface of fractured rectangular SLM sample. (f) Shear band interaction with a pore.

amorphous. More precisely, such heterogeneities in the amorphous state can be fluctuations in the local packing density or composition [56,59,60]. From this perspective, it is somewhat remarkable, that the shear bands propagate in a straight manner and are not affected by the layerwise processing, since this is a strong implication for the fact that the SLM samples are homogeneous even beyond the atomic level. Fig. 3(f) shows the macroscopic interaction between a pores and a propagating shear band. The shear band cuts through the pore, which is accompanied by a slight shift (offset) of the shear band propagation direction. Pores can be regarded as a second phase [61], which alter the stress concentration in the material during mechanical loading [62]. Large pores can, therefore, result in early failure [22]. Hence, further improvements in the relative density of additively manufactured BMGs by optimizing the processing parameters might lead to mechanical properties comparable to those of as-cast BMGs.

In order to study the macroscopic structural homogeneity of the SLM samples, microhardness measurements were performed on both SLM and as-cast $Zr_{52.5}Cu_{17.9}Ni_{14.6}Al_{10}Ti_5$ samples. Fig. 4 displays the respective microhardness maps of the cross and longitudinal section for SLM and as-cast samples. As shown in Fig. 4(a), the indents were created in the central part of the samples, where the laser works steadily in case of the SLM samples and where the cooling rate does not have a gradient as in case of the as-cast samples. All the microhardness maps in Fig. 6 show rather uniform values ranging from 496 ± 6 HV0.2 to 524 ± 6 HV0.2. When comparing the cross-section and the longitudinal section of the SLM sample (Figs. 4(b) and (c)), one finds that the hardness values are quite homogeneous across the entire sample. The microhardness measurements do not reveal any features, which could correspond to the heat-affected zone or the margins of a melt track [20,21]. Since no obvious differences in the hardness maps of the as-cast and SLM samples are present (Figs. 4(d) and (e)), the layer-by-layer processing method of SLM does not seem to significantly relax or rejuvenate the structure, which would otherwise result in higher or lower hardness values, respectively [56].

The sliding wear experiments were conducted to explore whether the manufacturing process affects the wear behaviour and the wear mechanisms. The coefficient of friction as a function of time for an as-cast specimen, is shown in Figs. 5(a) and (b). The coefficient of friction reaches a steady state with a value of about 0.4 within the first 35 min of testing. Between 35 and 120 min, the coefficient increases as does

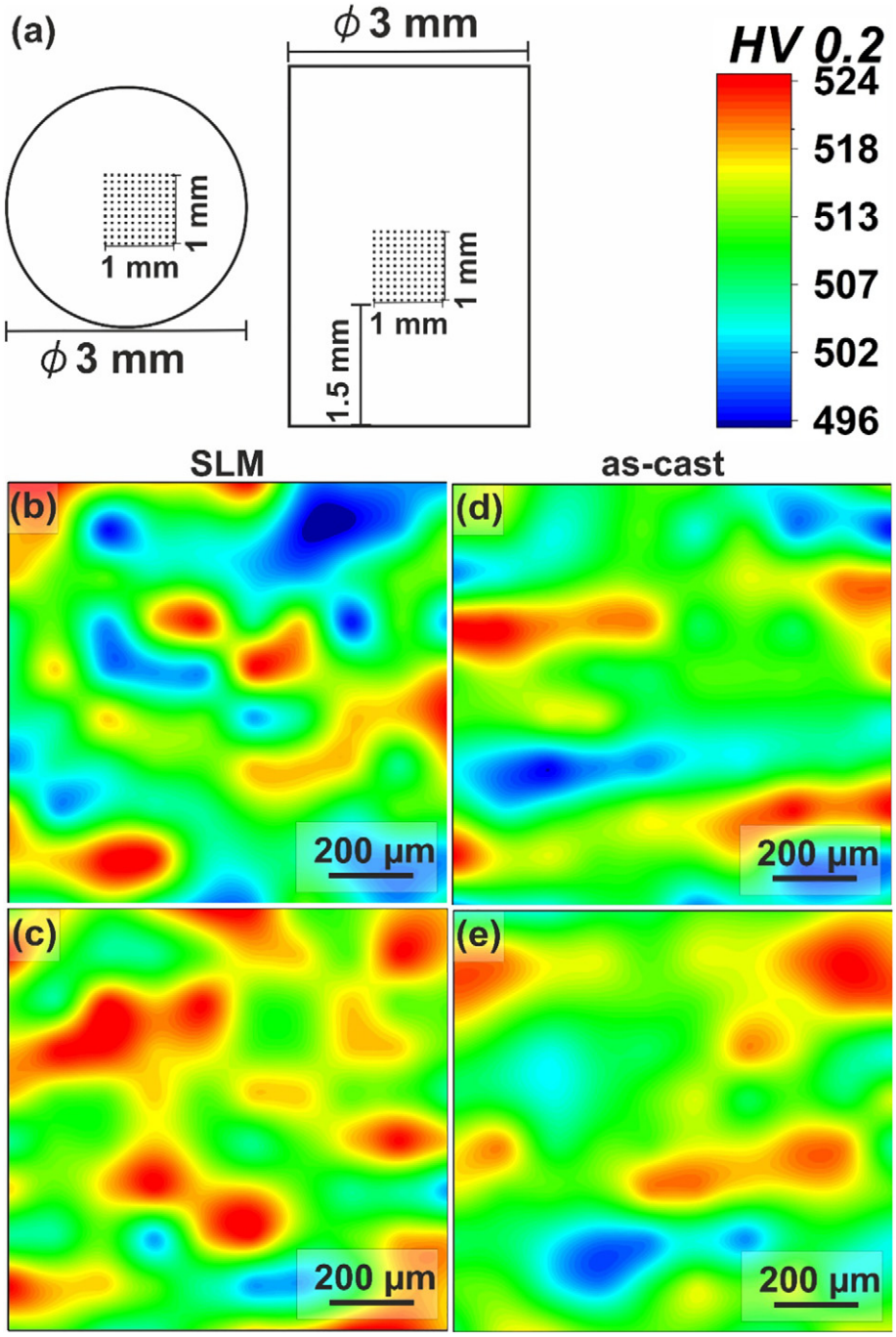

Fig. 4. (a) Schematic of the locations at which microhardness indents were placed on the cross and longitudinal sections of the samples. Panels (b) and (d) depict the microhardness contour maps for the cross section of SLM and the as-cast sample, respectively. Panels (c) and (e) display the microhardness maps for the longitudinal section of SLM and as-cast BMGs, respectively.

its scatter. This is indicative of a transformation in the wear mode [63]. The worn surfaces of the as-cast $Zr_{52.5}Cu_{17.9}Ni_{14.6}Al_{10}Ti_5$ glass after different sliding times are shown in Figs. 5 (c) to (f). Only slim grooves are visible (Fig. 5(c)) and their evolution indicates a distinct abrasive mechanism at the early stage of wear. With increasing sliding time, some fine debris forms (Fig. 5 (d)) and more material is ploughed out of the surface. This coincides with the drastic increase in the scattering of the coefficient of friction (Figs. 5(a) and (b)) and suggests a changing wear mode. Plastically deformed grooves and adhering debris can be observed at later stages of wear (Figs. 5(e) and (f)). The resulting typical mixed worn morphology indicates an abrasive and adhesive wear mechanism [32,63].

The coefficient of friction and the surfaces of the SLM samples at different stages of wear testing are illustrated in Fig. 6. The coefficient of friction (Figs. 6(a) and (b)) shows a similar trend like the as-cast specimen. Again, a change in the wear mode occurs after 35 min when the initial steady state ends. However, the fluctuations in the coefficient of friction after 80 min are more pronounced than for the as-cast sample and the maximum values are distinctly higher than for the as-cast glass. As long as the wear mode is purely abrasive (within the first 60 min), the worn surfaces of the SLM sample (Figs. 6(c) and (d)) cannot be distinguished from the as-cast sample. More but smaller regions of plastically deformed material are found at the later stages of wear ((Figs. 6(e) and (f)). The wear mode in metallic glasses has been

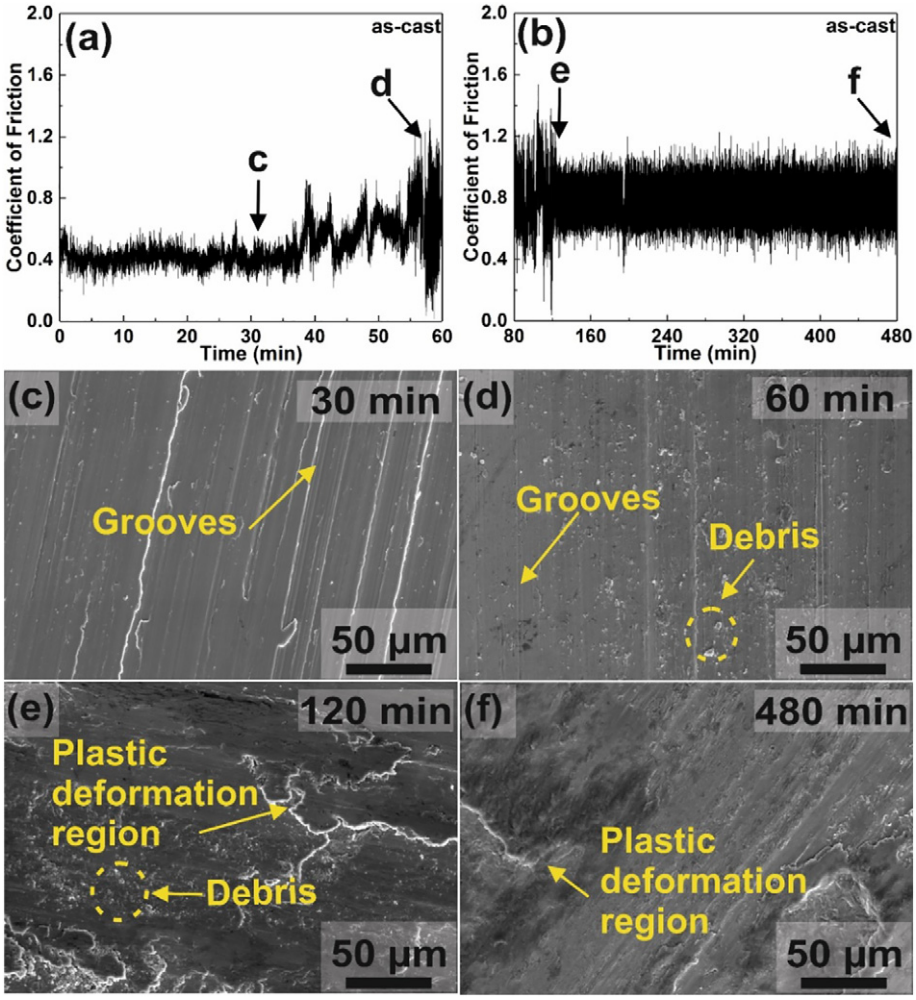

Fig. 5. (a) and (b) depict the coefficient of friction as a function of sliding time for the as-cast $Zr_{52.5}Cu_{17.9}Ni_{14.6}Al_{10}Ti_5$ sample. Its variation suggests a change in the wear mode. (c) to (f) show the morphologies of the worn surfaces after 30, 60, 120, 480 min of sliding. Grooves and debris can be clearly seen after the first 60 min (shown in (c) and (d)). In (e) and (f), plastically deformed regions dominate the surface.

reported to transform to the "brittle and ductile" mixed stage at the later stages of wear [24]. Thereby, the sample temperature can rise with test duration until crystallization occurs. Prior to that, coexisting softer and harder regions in the glass are expected to evolve during this mixed stage of wear [24] and they are reflected in a larger fluctuation of the coefficient of friction [24]. It is noteworthy that the scattering of the coefficient of friction is more pronounced for the SLM sample than for the as-cast material. This could be either related to the higher degree of porosity or to intrinsic structural heterogeneities on small length scales. The present microhardness measurements are incapable to reveal such small-scale heterogeneities because of their limited spatial resolution. A more detailed analysis would render nanoindentation necessary, which is beyond the scope of the present work.

The coefficient of friction plays an important role in determining the wear resistance. A smaller value generally indicates higher wear resistance. Fig. 7 (a) compares the average coefficient of friction for the SLM and the as-cast sample at different sliding times. The average coefficient increases with sliding time, also due to the varying wear mechanism. Even though the coefficient of friction distinctly scatters for the SLM samples, the average coefficient of friction (COF) is slightly lower than for the as-cast sample after long testing times (i.e. 480 min), indicating a slightly better wear resistance for the SLM sample. At the early and intermediate stages of wear testing, the average COF is comparable for both $Zr_{52.5}Cu_{17.9}Ni_{14.6}Al_{10}Ti_5$ samples (Fig. 7(a)). The specific wear rate for a SLM and an as-cast sample is shown in Fig. 7(b) and it can be calculated as follows:

$$K_w = \frac{V}{F \times L} \tag{1}$$

where K_w is the wear rate; V is the loss volume determined by $V = (m_o - m_w)/\rho$ where m_o and m_w is the mass prior to and after testing, respectively, ρ is the density of the material; F is the load applied on the sample; L is the sliding distance given by $L = 2\pi rvt$, where r is the radius of the wear track, v is the rotating speed and t is the sliding duration [29]. The trend of the time-dependent specific wear rate agrees with the average COF (Fig. 7(a)). Moreover, the wear rate for specimens prepared by the two different processing conditions is within the experimental error –at least for the early and intermediate stages of wear testing.

In the remainder of this work, we want to discuss the corrosion tests performed on as-cast BMGs and BMGs obtained by SLM. Fig. 8 shows the anodic polarization curves of selected SLM and as-cast $Zr_{52.5}Cu_{17.9}Al_{10}Ni_{14.6}Ti_5$ samples recorded in 0.01 M Na_2SO_4 + 0.1 M NaCl solution. Please note that the presented curves were selected as one representative from 5 to 7 independent measurements for each material state. The repeatability of the characteristic potential values is intrinsically limited. To account for the experimental error, the typical scattering of corrosion potential (ΔE_{corr}), pitting potential(ΔE_{pit})and repassivation potential (ΔE_R) are indicated in the plot. While ΔE_{corr} must be mainly ascribed to the individual history of each prepared

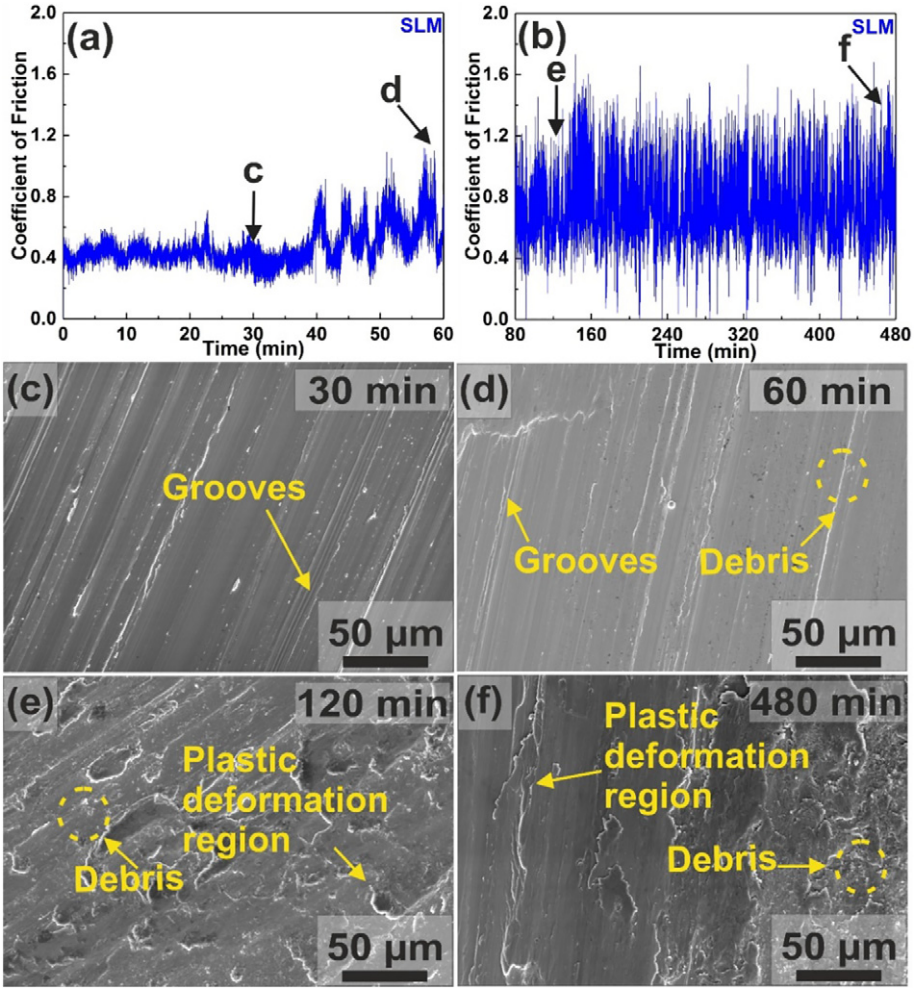

Fig. 6. (a) and (b) display the coefficient of friction for the $Zr_{52.5}Cu_{17.9}Ni_{14.6}Al_{10}Ti_5$ sample produced by SLM. A similar trend as in panels (a) and (b) becomes obvious. Panels (c) to (f) show the SEM images of the worn surfaces after 30, 60, 120, 480 min of wear testing. The SLM samples exhibit a comparable wear performance as the as-cast samples.

sample surface, ΔE_{pit} and ΔE_R may be indicative for the manufacturing-related pitting susceptibility and repassivation ability of the different sample types [64].

The air-aged as-cast sample state reveals upon initial polarization very low corrosion current densities, i_{corr} (determined by graphical Tafel extrapolation) on the order of 0.005 μA/cm^2 at E_{corr} values ranging from −0.23 to −0.35 V vs. SCE [65]. This results from the beginning oxide formation upon air exposure and immersion in the electrolyte under OCP conditions. The current density increases gradually up to 2 μA/cm^2 during anodic polarization. Consequently, the corrosive dissolution is rather low and it is superimposed by the anodic growth of passive films with a strong barrier-type effect [38,64]. A sudden steep rise

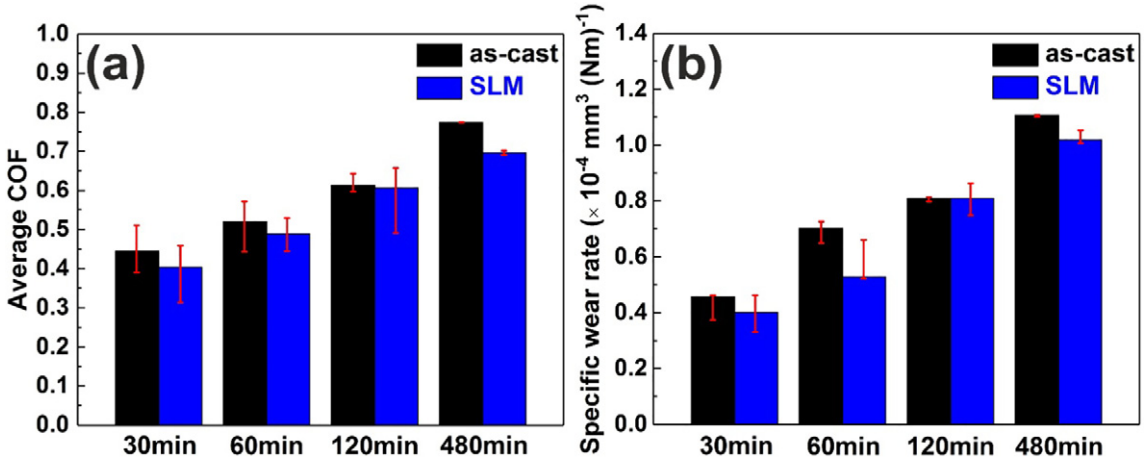

Fig. 7. (a) Average coefficient of friction (COF) of the $Zr_{52.5}Cu_{17.9}Ni_{14.6}Al_{10}Ti_5$ SLM and as-cast samples as a function of time. The COF-values for samples prepared by both process conditions are similar except for the longest testing duration. (b) The specific wear rate of the SLM and as-cast specimen. The wear rate is in high agreement with the average COF (shown in panel (a)).

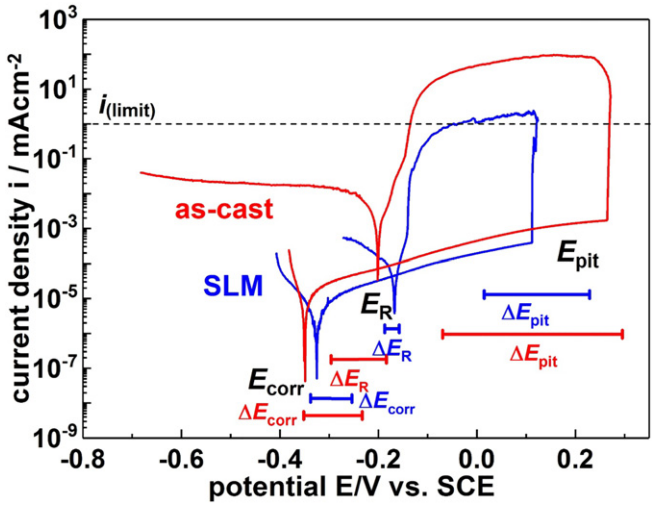

Fig. 8. Anodic polarization curves recorded for $Zr_{52.5}Cu_{17.9}Ni_{14.6}Al_{10}Ti_5$ SLM and as-cast samples in 0.01 M Na_2SO_4 + 0.1 M NaCl solution. Corrosion potential (ΔE_{corr}), pitting potential (ΔE_{pit}) and repassivation potential (ΔE_R) bars represent the scattering of the values within 5–7 independent measurements. Both samples show similar corrosion behaviour. The SLM sample performs slightly better than the as-cast sample during pitting corrosion.

of the anodic current density at E_{pit} is due to local passive film breakdown, pit initiation and rapid pit growth [38]. A significant overshoot of the real current density above the current density limit of 1 mA/cm^2, which was set as threshold value to reverse the polarization direction for surface repassivation, as well as a very wide potential range in the reverse scan with a quite high current density correspond to a very strong pit propagation into the glassy matrix and a very limited surface healing ability. Since the reverse scanning of the potential reduces the driving force for anodic dissolution, the current density drops and a second minimum at E_R occurs reflecting repassivation of the previously damaged surface. The underlying surface reaction mechanisms were in detail described in previous works [34–38]. As the local breakdown of the very thin passive film on the sample surface (= excavated sample cross section) is a more or less random event, which mainly depends on the number, distribution and nature of defects in the BMG, the E_{pit}-value strongly varies across independent measurements of different as-cast samples and results in a rather large ΔE_{pit}. By contrast, the following strong current density hysteresis and the subsequent minimum at E_R show a much better repeatability. Once the sensitive pit initiation took place, the following pit growth and repassivation steps proceed at quite similar rates for all cast sample states of the considered alloy.

The polarization curves of the samples prepared by SLM reveal quite a similar overall behaviour with characteristic steps described above for the as-cast BMG samples. However, the variation of the pitting potential, ΔE_{pit}, is less pronounced reflecting a more narrow potential range of passive film breakdown and pit initiation. Furthermore, the current density overshoot above the set limit is much smaller and during reverse scanning the current density plateau is lower and the minimum of E_R is reached at more positive potentials. These facts indicate a somewhat less pronounced pit propagation rate and easier surface repassivation [34,38,64].

Altogether, this indicates a slightly reduced pitting corrosion susceptibility and slightly improved surface healing ability for BMGs prepared by SLM. This could be related to a better homogeneity in comparison to as-cast BMGs of the same composition. Yet, these differences appear to be rather subtle and it is challenging to try to identify those by conventional chemical analysis or electron microscopy.

After the corrosion tests, the surfaces were investigated in a scanning electron microscope to better understand the degradation phenomena. Fig. 9 shows the surface morphologies of damaged cross-sectional regions of an as-cast (Fig. 9 (a)) and an additively manufactured BMG sample (Fig. 9 (b)), respectively. The principal damage morphology is for both sample types similar and points to similar local corrosion processes, which are well described for this glassy alloy type synthesized by casting [36]. In case of the cast material, three individual pits with diameters between 30 and 50 μm with irregular edges and rather rough walls are shown in Fig. 9 (a). The size of a pit on a SLM sample cross section, in contrast, reaches dimensions of about 200 μm (Fig. 9 (b)). One can also detect small cracks and openings, which are similar to features observed for the corroded as-cast sample. The pit walls of the SLM sample show "honeycomb micromesh"-like regions, which is typical after repassivation [34]. The openings in the bottom of both sample types indicate that strong local dissolution occurs deep below the cross-sectional surface. The cavity morphology of the damages can catalyse the corrosion process since it can provide a shortcut for the electrolyte and thus, enabling local enrichment of chloride ions and acidification.

This preliminary comparison between the corrosion behaviour of additively manufactured and cast $Zr_{52.5}Cu_{17.9}Ni_{14.6}Al_{10}Ti_5$ glass in a selected electrolyte suggests that the structural defects typically occurring in as-cast samples are more detrimental for the corrosion stability than the pore-type defects, which are characteristic of SLM samples. While the former represent chemical discontinuities with sharp phase boundaries to the glassy matrix, the latter are geometrical discontinuities yielding a lower driving force for the chloride attack resulting in pit initiation and propagation. This can be seen similar to findings from earlier studies, i.e. that mechanically induced defects such as microindents have to exceed a certain critical size to become preferred pit initiation sites rather than crystals at the same glassy sample cross-section [36].

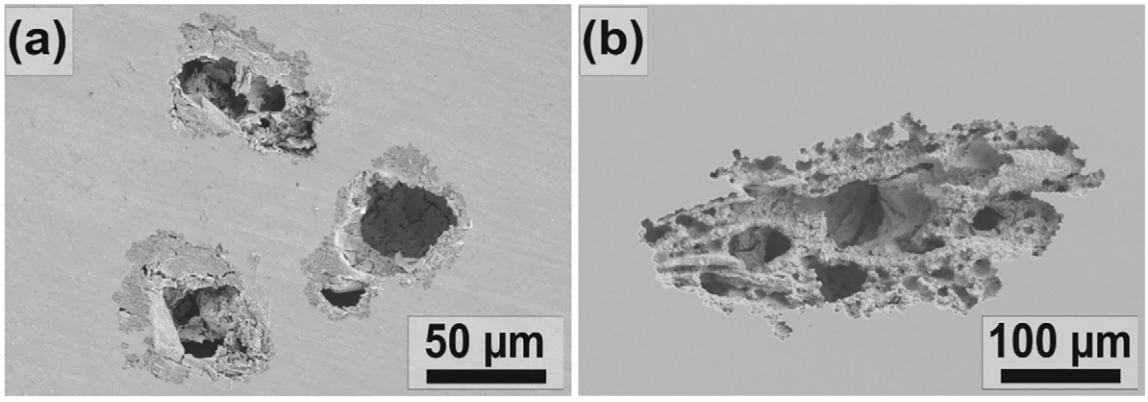

Fig. 9. Surface morphologies of $Zr_{52.5}Cu_{17.9}Ni_{14.6}Al_{10}Ti_5$ as-cast sample (a) and SLM sample (b) after repassivation. Pits formed during linear anodic polarization to pitting potential (E_{pit}) and reverse scanning to repassivation potential (E_R). The as-cast sample has more but smaller pitted regions than the SLM sample. Both samples show rough pit walls.

However, besides their nature also the number and distribution of defects throughout the sample volume is decisive. Therefore, a more comprehensive corrosion study is needed to fully clarify the impact of the manufacturing route on the corrosion mechanism and the overall corrosion properties for glassy alloys.

4. Conclusions

The present study demonstrates that bulk glassy $Zr_{52.5}Cu_{17.9}Ni_{14.6}Al_{10}Ti_5$ samples can be produced via selective laser melting (SLM). Their relative density reaches values above 98.7%. Compared to the yield strength of as-cast BMGs (about 1830 MPa), additively manufactured BMGs yield at lower stresses of about 1710 MPa. A limited but detectable plastic strain (about 0.5%) after yielding was determined for all SLM specimens, which is still lower than for the as-cast glass of identical composition. The residual porosity in the SLM samples is believed to be responsible for the premature failure of the BMGs prepared by selective laser melting. Careful process optimization might even results in raising the plastic strain to the values found in the cast glass. Nonetheless, the effect of these pores on the microhardness is negligible and the hardness values of SLM samples and as-cast samples have similar distributions. The complex thermal history of the SLM samples, thus, has no evident influence on the microhardness. A similar wear performance for SLM and as-cast BMG specimens can be deduced from the time-dependent coefficients of friction, wear rates and surface morphologies after wear. In other words, SLM processing has no negative effect on these mechanical properties. Finally, the comparable anodic polarization curves and pitting behaviour of the SLM and as-cast samples suggest that they have a similar corrosion resistance. The slightly improved surface healing ability and reduced pitting corrosion susceptibility is an advantage inherent in SLM BMGs and could originate from a chemically more uniform glassy structure.

In other words, the BMGs produced by selective laser melting demonstrate wear and corrosion resistance, which are very similar to as-cast BMGs. Even though the plastic strain is still limited, the present findings prove that additively manufactured metallic glasses can deform plastically on compressive loading. Careful process optimization might allow for plastic strains comparable to those found in as-cast glasses. Our comprehensive investigations reveal that powder bed fusion, such as selective laser melting, is a suitable and powerful tool for designing new and sophisticated geometries consisting of amorphous alloys. This approach could open the door to new applications for this metastable material, especially such applications, which require long-term durability in corrosive environments.

CRediT authorship contribution statement

L. Deng: Conceptualization, Validation, Investigation, Resources, Formal analysis, Visualization, Writing - original draft. **A. Gebert:** Investigation, Writing - review & editing, Resources. **L. Zhang:** Investigation. **H.Y. Chen:** Resources. **D.D. Gu:** Resources. **U. Kühn:** Resources, Supervision. **M. Zimmermann:** Supervision. **K. Kosiba:** Writing - original draft. **S. Pauly:** Conceptualization, Writing - review & editing, Supervision.

Declaration of competing interest

The authors declare that they have no known competing financial interests or personal relationships that could have appeared to influence the work reported in this paper.

Acknowledgements

P. Xue and S. Scudino are thanked for insightful discussions. Moreover, valuable technical support by A. Schultze, M. Johne, A. Voß, H. Bußkamp, B. Bartusch, S. Donath and H. Merker is appreciated. L. Deng acknowledges financial support by the Chinese Scholarship Council (CSC). S. Pauly and K. Kosiba acknowledge support by German Science Foundation (DFG) under grant nos. PA 2275/6-1 and KO5771/1-1.

Data availability

The data supporting the findings of this study are available from the corresponding author on reasonable request.

References

[1] C.Y. Yap, C.K. Chua, Z.L. Dong, Z.H. Liu, D.Q. Zhang, L.E. Loh, S.L. Sing, Review of selective laser melting: materials and applications, Appl. Phys. Rev. 2 (2015), 041101.
[2] L.C. Zhang, H. Attar, Selective laser melting of titanium alloys and titanium matrix composites for biomedical applications: a review, Adv. Eng. Mater. 18 (2016) 463–475.
[3] S. Pauly, P. Wang, U. Kühn, K. Kosiba, Experimental determination of cooling rates in selectively laser-melted eutectic Al-33Cu, Addit. Manuf. 22 (2018) 753–757.
[4] K. Prashanth, H.S. Shahabi, H. Attar, V. Srivastava, N. Ellendt, V. Uhlenwinkel, J. Eckert, S. Scudino, Production of high strength $Al_{85}Nd_8Ni_5Co_2$ alloy by selective laser melting, Addit. Manuf. 6 (2015) 1–5.
[5] E. Williams, N. Lavery, Laser processing of bulk metallic glass: a review, J. Mater. Process. Tech. 247 (2017) 73–91.
[6] Y. Li, Y. Shen, M.C. Leu, H.-L. Tsai, Building Zr-based metallic glass part on Ti-6Al-4V substrate by laser-foil-printing additive manufacturing, Acta Mater. 144 (2018) 810–821.
[7] A. Inoue, Stabilization of metallic supercooled liquid and bulk amorphous alloys, Acta Mater. 48 (2000) 279–306.
[8] H. Attar, L. Löber, A. Funk, M. Calin, L. Zhang, K. Prashanth, S. Scudino, Y. Zhang, J. Eckert, Mechanical behavior of porous commercially pure Ti and Ti–TiB composite materials manufactured by selective laser melting, Mater. Sci. Eng. A 625 (2015) 350–356.
[9] S. Pauly, L. Löber, R. Petters, M. Stoica, S. Scudino, U. Kühn, J. Eckert, Processing metallic glasses by selective laser melting, Mater. Today 16 (2013) 37–41.
[10] X. Li, M. Roberts, S. O'Keeffe, T. Sercombe, Selective laser melting of Zr-based bulk metallic glasses: processing, microstructure and mechanical properties, Mater. Des. 112 (2016) 217–226.
[11] S. Pauly, C. Schricker, S. Scudino, L. Deng, U. Kühn, Processing a glass-forming Zr-based alloy by selective laser melting, Mater. Des. 135 (2017) 133–141.
[12] L. Deng, S. Wang, P. Wang, U. Kühn, S. Pauly, Selective laser melting of a Ti-based bulk metallic glass, Mater. Lett. 212 (2018) 346–349.
[13] N. Li, J. Zhang, W. Xing, D. Ouyang, L. Liu, 3D printing of Fe-based bulk metallic glass composites with combined high strength and fracture toughness, Mater. Des. 143 (2018) 285–296.
[14] P. Bordeenithikasem, M. Stolpe, A. Elsen, D.C. Hofmann, Glass forming ability, flexural strength, and wear properties of additively manufactured Zr-based bulk metallic glasses produced through laser powder bed fusion, Addit. Manuf. 21 (2018) 312–317.
[15] X. Lin, Y. Zhang, G. Yang, X. Gao, Q. Hu, J. Yu, L. Wei, W. Huang, Microstructure and compressive/tensile characteristic of large size Zr-based bulk metallic glass prepared by laser solid forming, J. Mater. Sci. Technol. 35 (2019) 328–335.
[16] D.C. Hofmann, P. Bordeenithikasem, A. Pate, S.N. Roberts, E. Vogli, Developing processing parameters and characterizing microstructure and properties of an additively manufactured FeCrMoBC metallic glass forming alloy, Adv. Eng. Mater. 20 (2018), 1800433.
[17] X. Li, C. Kang, H. Huang, L. Zhang, T.B. Sercombe, Selective laser melting of an Al86Ni6Y4. 5Co2La1. 5 metallic glass: processing, microstructure evolution and mechanical properties, Mater. Sci. Eng. A 606 (2014) 370–379.
[18] C. Zhang, X.-m. Li, S.-Q. Liu, H. Liu, L.-J. Yu, L. Liu, 3D printing of Zr-based bulk metallic glasses and components for potential biomedical applications, J. Alloys Comp. 790 (2019) 963–973.
[19] D. Ouyang, N. Li, W. Xing, J. Zhang, L. Liu, 3D printing of crack-free high strength Zr-based bulk metallic glass composite by selective laser melting, Intermetallics 90 (2017) 128–134.
[20] J.P. Best, Z. Evenson, F. Yang, A.-C. Dippel, M. Stolpe, O. Gutowski, M.T. Hasib, X. Li, J.J. Kruzic, Structural periodicity in laser additive manufactured Zr-based bulk metallic glass, Appl. Phys. Lett. 115 (2019), 031902.
[21] D. Ouyang, N. Li, L. Liu, Structural heterogeneity in 3D printed Zr-based bulk metallic glass by selective laser melting, J. Alloys Comp. 740 (2018) 603–609.
[22] A. Greer, Y. Cheng, E. Ma, Shear bands in metallic glasses, Mater. Sci. Eng. R 74 (2013) 71–132.
[23] Z. Zhang, G. He, J. Eckert, L. Schultz, Fracture mechanisms in bulk metallic glassy materials, Phys. Rev. Lett. 91 (2003), 045505.
[24] M. Rahaman, L. Zhang, H. Ruan, Understanding the friction and wear mechanisms of bulk metallic glass under contact sliding, Wear 304 (2013) 43–48.
[25] A. Greer, K. Rutherford, I. Hutchings, Wear resistance of amorphous alloys and related materials, Int. Mater. Rev. 47 (2002) 87–112.
[26] D.R. Maddala, A. Mubarok, R.J. Hebert, Sliding wear behavior of $Cu_{50}Hf_{41.5}Al_{8.5}$ bulk metallic glass, Wear 269 (2010) 572–580.
[27] M. Ishida, H. Takeda, N. Nishiyama, K. Kita, Y. Shimizu, Y. Saotome, A. Inoue, Wear resistivity of super-precision microgear made of Ni-based metallic glass, Mater. Sci. Eng. A 449 (2007) 149–154.
[28] C. Tam, C. Shek, Abrasive wear of $Cu_{60}Zr_{30}Ti_{10}$ bulk metallic glass, Mater. Sci. Eng. A 384 (2004) 138–142.

[29] Y. Huang, H. Fan, D. Wang, Y. Sun, F. Liu, J. Shen, J. Sun, J. Mi, The effect of cooling rate on the wear performance of a ZrCuAlAg bulk metallic glass, Mater. Des. 58 (2014) 284–289.
[30] M.E. Siegrist, E.D. Amstad, J.F. Löffler, Tribological properties of graphite-and ZrC-reinforced bulk metallic glass composites, Intermetallics 15 (2007) 1228–1236.
[31] Y. Wang, H. Li, Y. Cheng, Y. Zheng, L. Ruan, In vitro and in vivo studies on Ti-based bulk metallic glass as potential dental implant material, Mater. Sci. Eng. C 33 (2013) 3489–3497.
[32] M. Rahaman, L. Zhang, M. Liu, W. Liu, Surface roughness effect on the friction and wear of bulk metallic glasses, Wear 332 (2015) 1231–1237.
[33] M. Rahaman, L. Zhang, H. Ruan, Effects of environmental temperature and sliding speed on the tribological behaviour of a Ti-based metallic glass, Intermetallics 52 (2014) 36–48.
[34] U.K. Mudali, S. Baunack, J. Eckert, L. Schultz, A. Gebert, Pitting corrosion of bulk glass-forming zirconium-based alloys, J. Alloys Comp. 377 (2004) 290–297.
[35] J.R. Scully, A. Gebert, J.H. Payer, Corrosion and related mechanical properties of bulk metallic glasses, J. Mater. Res. 22 (2007) 302–313.
[36] A. Gebert, P. Gostin, M. Uhlemann, J. Eckert, L. Schultz, Interactions between mechanically generated defects and corrosion phenomena of Zr-based bulk metallic glasses, Acta Mater. 60 (2012) 2300–2309.
[37] J. Paillier, C. Mickel, P.F. Gostin, A. Gebert, Characterization of corrosion phenomena of Zr–Ti–Cu–Al–Ni metallic glass by SEM and TEM, Mater. Charact. 61 (2010) 1000–1008.
[38] P.F. Gostin, D. Eigel, D. Grell, J. Eckert, E. Kerscher, A. Gebert, Comparing the pitting corrosion behavior of prominent Zr-based bulk metallic glasses, J. Mater. Res. 30 (2015) 233–241.
[39] L. Huang, Y. Yokoyama, W. Wu, P.K. Liaw, S. Pang, A. Inoue, T. Zhang, W. He, Ni-free Zr–Cu–Al–Nb–Pd bulk metallic glasses with different Zr/Cu ratios for biomedical applications, J. Biome. Mater. Res. Part B 100 (2012) 1472–1482.
[40] W. Peter, R. Buchanan, C. Liu, P. Liaw, M. Morrison, J. Horton, C. Carmichael Jr., J. Wright, Localized corrosion behavior of a zirconium-based bulk metallic glass relative to its crystalline state, Intermetallics 10 (2002) 1157–1162.
[41] A. Gebert, K. Mummert, J. Eckert, L. Schultz, A. Inoue, Electrochemical investigations on the bulk glass forming $Zr_{55}Cu_{30}Al_{10}Ni_5$ alloy, Mater. Corros. 48 (1997) 293–297.
[42] K. Mondal, B. Murty, U. Chatterjee, Electrochemical behavior of multicomponent amorphous and nanocrystalline Zr-based alloys in different environments, Corros. Sci. 48 (2006) 2212–2225.
[43] A. Kawashima, W.-P. Yu, B.-P. Zhang, H. Habazaki, K. Asami, K. Hashimoto, Pitting corrosion of amorphous Ni–Zr alloys in chloride ion containing sulfuric acid solutions, Mater. Trans. JIM 38 (1997) 443–450.
[44] S. Gravano, S. Torchio, F. Mazza, E. Angelini, M. Baricco, The effects of quenching conditions on the electrochemical behaviour of $Fe_{34}Ni_{36}Cr_{10}P_{14}B_6$ amorphous alloys, Corros. Sci. 33 (1992) 1227–1241.
[45] R. Dutta, G. Dey, Effects of partial crystallinity and quenched-in defects on corrosion of a rapidly solidified Ti-cu alloy, Bull. Mater. Sci. 26 (2003) 477–482.
[46] P. Wang, L. Deng, K. Prashanth, S. Pauly, J. Eckert, S. Scudino, Microstructure and mechanical properties of Al-cu alloys fabricated by selective laser melting of powder mixtures, J. Alloys Comp. 735 (2018) 2263–2266.
[47] X. Nie, X. Yang, L. Chen, K. Yeap, K. Zeng, D. Li, J. Pan, X. Wang, Q. Cao, S. Ding, The effect of oxidation on the corrosion resistance and mechanical properties of a Zr-based metallic glass, Corros. Sci. 53 (2011) 3557–3565.
[48] I.-C. Choi, Y. Zhao, Y.-J. Kim, B.-G. Yoo, J.-Y. Suh, U. Ramamurty, J. Jang, Indentation size effect and shear transformation zone size in a bulk metallic glass in two different structural states, Acta Mater. 60 (2012) 6862–6868.
[49] W.H. Wang, Roles of minor additions in formation and properties of bulk metallic glasses, Prog. Mater. Sci. 52 (2007) 540–596.
[50] Z.P. Lu, H. Bei, Y. Wu, G. Chen, E. George, C. Liu, Oxygen effects on plastic deformation of a Zr-based bulk metallic glass, Appl. Phys. Lett. 92 (2008) 011915.
[51] A. Simchi, The role of particle size on the laser sintering of iron powder, Metallurgical and Mater. Trans. B 35 (2004) 937–948.
[52] H. Zhu, J. Fuh, L. Lu, The influence of powder apparent density on the density in direct laser-sintered metallic parts, Int. J. Mach. Tools Manuf. 47 (2007) 294–298.
[53] A. Kündig, M. Ohnuma, T. Ohkubo, K. Hono, Early crystallization stages in a Zr–Cu–Ni–Al–Ti metallic glass, Acta Mater. 53 (2005) 2091–2099.
[54] L. He, Z. Wu, F. Jiang, J. Sun, Enhanced thermal stability of $Zr_{65}Cu_{17.5}Ni_{10}Al_{7.5}$ metallic glass at temperature range near glass transition by oxygen impurity, J. Alloys Comp. 456 (2008) 181–186.
[55] S. Scudino, K.B. Surreddi, G. Wang, G. Liu, Effect of stress concentration on plastic deformation of $Zr_{41.2}Ti_{13.8}Cu_{12.5}Ni_{10}Be_{22.5}$ bulk metallic glass under compressive loading, Mater. Lett. 179 (2016) 202–205.
[56] K. Kosiba, D. Şopu, S. Scudino, L. Zhang, J. Bednarcik, S. Pauly, Modulating heterogeneity and plasticity in bulk metallic glasses: role of interfaces on shear banding, Int. J. Plasticity 119 (2019) 156–170.
[57] S. Scudino, J. Bian, H.S. Shahabi, D. Şopu, J. Sort, J. Eckert, G. Liu, Ductile bulk metallic glass by controlling structural heterogeneities, Sci. Rep. 8 (2018) 9174.
[58] D. Şopu, A. Stukowski, M. Stoica, S. Scudino, Atomic-level processes of shear band nucleation in metallic glasses, Phys. Rev. Lett. 119 (2017), 195503.
[59] H. Wagner, D. Bedorf, S. Küchemann, M. Schwabe, B. Zhang, W. Arnold, K. Samwer, Local elastic properties of a metallic glass, Nat. Mater. 10 (2011) 439.
[60] K. Kim, J. Das, F. Baier, M. Tang, W. Wang, J. Eckert, Heterogeneity of a $Cu_{47.5}Zr_{47.5}Al_5$ bulk metallic glass, Appl. Phys. Lett. 88 (2006) 051911.
[61] K. Kosiba, S. Scudino, R. Kobold, U. Kühn, A. Greer, J. Eckert, S. Pauly, Transient nucleation and microstructural design in flash-annealed bulk metallic glasses, Acta Mater. 127 (2017) 416–425.
[62] F. Shimizu, S. Ogata, J. Li, Yield point of metallic glass, Acta Mater. 54 (2006) 4293–4298.
[63] H. Wu, I. Baker, Y. Liu, X. Wu, P.R. Munroe, J. Zhang, Tribological studies of a Zr-based bulk metallic glass, Intermetallics 35 (2013) 25–32.
[64] A. Gebert, P. Gostin, L. Schultz, Effect of surface finishing of a Zr-based bulk metallic glass on its corrosion behaviour, Corros. Sci. 52 (2010) 1711–1720.
[65] E. McCafferty, Validation of corrosion rates measured by the Tafel extrapolation method, Corros. Sci. 47 (2005) 3202–3215.